


## Article

# Synthesizing the High Surface Area g-C<sub>3</sub>N<sub>4</sub> for Greatly Enhanced Hydrogen Production

Chengfei Wang <sup>1</sup>, Tongxin Han <sup>2</sup>, Chang Xin <sup>2</sup> and Hui Miao <sup>2,\*</sup> 

<sup>1</sup> College of Urban and Environmental Sciences, Northwest University, Xi'an 710127, China; wangchengfei@stumail.nwu.edu.cn

<sup>2</sup> School of Physics, Northwest University, Xi'an 710127, China; hantongxin@stumail.nwu.edu.cn (T.H.); xinchang@stumail.nwu.edu.cn (C.X.)

\* Correspondence: huim@nwu.edu.cn

**Abstract:** Adjusting the structure of g-C<sub>3</sub>N<sub>4</sub> to significantly enhance its photocatalytic activity has attracted considerable attention. Herein, a novel, sponge-like g-C<sub>3</sub>N<sub>4</sub> with a porous structure is prepared from the annealing of protonated melamine under N<sub>2</sub>/H<sub>2</sub> atmosphere (PH-CN). Compared to bulk g-C<sub>3</sub>N<sub>4</sub> via calcination of melamine under ambient atmosphere (B-CN), PH-CN displays thinner nanosheets and a higher surface area (150.1 m<sup>2</sup>/g), which is a benefit for shortening the diffusion distance of photoinduced carriers, providing more active sites, and finally favoring the enhancement of the photocatalytic activity. Moreover, it can be clearly observed from the UV-vis spectrum that PH-CN displays better performance for harvesting light compared to B-CN. Additionally, the PH-CN is prepared with a larger band gap of 2.88 eV with the Fermi level and conduction band potential increased and valence band potential decreased, which could promote the water redox reaction. The application experiment results show that the hydrogen evolution rate on PH-CN was nearly 10 times higher than that of B-CN, which was roughly 4104 μmol h<sup>-1</sup> g<sup>-1</sup>. The method shown in this work provides an effective approach to adjust the structure of g-C<sub>3</sub>N<sub>4</sub> with considerable photocatalytic hydrogen evolution activity.

**Keywords:** g-C<sub>3</sub>N<sub>4</sub>; photocatalytic hydrogen evolution; protonation; N<sub>2</sub>/H<sub>2</sub> atmosphere



**Citation:** Wang, C.; Han, T.; Xin, C.; Miao, H. Synthesizing the High Surface Area g-C<sub>3</sub>N<sub>4</sub> for Greatly Enhanced Hydrogen Production. *Catalysts* **2021**, *11*, 832. <https://doi.org/10.3390/catal11070832>

Academic Editor:  
Ekaterina A. Kozlova

Received: 18 June 2021  
Accepted: 6 July 2021  
Published: 8 July 2021

**Publisher's Note:** MDPI stays neutral with regard to jurisdictional claims in published maps and institutional affiliations.



**Copyright:** © 2021 by the authors. Licensee MDPI, Basel, Switzerland. This article is an open access article distributed under the terms and conditions of the Creative Commons Attribution (CC BY) license (<https://creativecommons.org/licenses/by/4.0/>).

## 1. Introduction

Driven by the increasing need for clean and environmental-friendly energy, hydrogen, regarded as a storable and clean fuel, is potentially considered one of the most reliable energy carriers due to its high-energy capacity. Hydrogen can be produced from a wide range of resources by using different feedstock, pathways, and technologies, including fossil fuels and renewable energy resources [1]. The hydrogen production pathway depends on three elements: the material containing hydrogen, an energy source, and catalyst material [2]. It would be of great use for a carbon-neutral and sustainable society if hydrogen could be produced from renewable energy resources, such as solar energy [3]. Photocatalytic hydrogen production via water splitting represents one of the most promising but challenging techniques for sustainable solar energy storage. Since the pioneering report by Fujishima and Honda in 1972, TiO<sub>2</sub> has been used as a photoelectrode for sustainable hydrogen production via water splitting [4]. Semiconductor photocatalytic techniques are considered to be ideal methods to convert solar energy into hydrogen [5–7]. In recent decades, many efforts have been devoted to synthesis and regulation of a variety semiconductor materials, such as g-C<sub>3</sub>N<sub>4</sub> [8], Ta<sub>3</sub>N<sub>5</sub> [9], TiO<sub>2</sub> [10], ZnO [11], etc. Attaining highly active solar-driven photocatalytic reactions for these traditional nitrides and oxides photocatalysts without noble metal cocatalysts is still a challenge. Recently, Yusuke et al. [10] reported a cocatalyst-free rutile TiO<sub>2</sub> via band shape engineering with exceptional solar hydrogen production. In situ, photogenerated Ti<sup>3+</sup> can act as a cocatalyst, which could promote the hydrogen evolution reaction dynamics and provide a new insight into in situ photogenerated metal

cations as cocatalysts. Another challenge is how to effectively improve the surface area with more active sites exposed and more water molecules adsorbed.

Graphite carbon nitride ( $g\text{-C}_3\text{N}_4$ ), which is the most stable allotrope of carbon nitride, has triggered broad interest due to its many fascinating properties, namely superior thermal and chemical stability, an appropriate direct band gap of 2.7 eV, and its low cost due to its abundant existence. These advantages lead to several applications such as  $\text{CO}_2$  reduction [12–15], water splitting [16–19], organic pollution degradation [20–22], etc. However, obtained bulk  $g\text{-C}_3\text{N}_4$  prepared via the common thermal polymerization method has suffered from multiple drawbacks from achieving high activity, such as its small specific surface area and high charge recombination rate [23]. Until now, considerable strategies have been used to optimize the photocatalytic performance of the bulk  $g\text{-C}_3\text{N}_4$  by adjusting its structure and its optical and electronic properties [24–27]. Gong et al. [28] reported a template-free synthesis of nanocage-like  $g\text{-C}_3\text{N}_4$  with a high surface area and nitrogen defects by firstly hydrothermal treatment of the dicyandiamide and then direct calcination. Liu et al. [29] synthesized a defective ultra-thin two-dimensional  $g\text{-C}_3\text{N}_4$ , first by calcination of the initial material ammonium chloride and melamine and then by annealing under Ar atmosphere. Nevertheless, improving the photocatalysis properties of  $g\text{-C}_3\text{N}_4$  is still desirable.

Herein, we have successfully synthesized sponge-like  $g\text{-C}_3\text{N}_4$  nanosheets by annealing the protonated melamine under  $\text{N}_2/\text{H}_2$  atmosphere (PH-CN); the porous structure  $g\text{-C}_3\text{N}_4$  nanosheets via calcination of the protonated melamine under ambient atmosphere (P-CN); the  $g\text{-C}_3\text{N}_4$  nanosheets via annealing of the melamine under  $\text{N}_2/\text{H}_2$  atmosphere (H-CN); and bulk  $g\text{-C}_3\text{N}_4$  via calcination of the melamine under ambient atmosphere (B-CN). The optimized product PH-CN displayed greatly enhanced photocatalytic activity of hydrogen evolution and outstanding stability compared to B-CN. Moreover, the specific surface area, porosity, charge pairs separation property, and conduction band potential for hydrogen production have been carefully investigated.

## 2. Results and Discussion

### 2.1. XRD Pattern of the Prepared Samples

Figure 1 shows the X-ray diffraction patterns of the prepared samples. In all XRD profiles, there are two distinct peaks at  $13.3^\circ$  and  $27.1^\circ$ , which resulted from the interplanar peaks of the in-plane structural packing motif and the stacked layer of the aromatic systems, which correspond to the (100) and (002) crystal planes, respectively. For (100) crystal plane, it can be clearly observed that the peaks of P-CN and PH-CN are weaker than those of B-CN and H-CN, indicating that the protonation of melamine destroyed the in-plane structural repeating motifs of the aromatic systems, thus making the peak almost disappear [25]. Moreover, the weaker peak at  $27.1^\circ$  for (002) crystal plane in PH-CN, compared to B-CN, indicates that the PH-CN possesses fewer stacked  $g\text{-C}_3\text{N}_4$  layers.

### 2.2. SEM Pattern of the Prepared Samples

In order to confirm the microstructures and morphologies of the obtained samples, scanning electron microscopy (SEM) was introduced in Figure 2. As shown in Figure 2a, the B-CN exhibited an irregularly aggregated architecture with multiple stacking layers. In Figure 2b, the H-CN shows a loosened structure compared to the B-CN, which was denser and more aggregated. In Figure 2c, the resultant P-CN shows a partially porous structure, while some part of the sample still remains in the nanosheet framework. In Figure 2d, the obtained PH-CN sample shows a highly porous and loosened microstructure. The above observation indicates that the B-CN started to be exfoliated into nanosheets (H-CN) when the annealing of melamine took place under  $\text{N}_2/\text{H}_2$  atmosphere. The  $\text{N}_2/\text{H}_2$  atmosphere could restrain the stacked  $g\text{-C}_3\text{N}_4$  layers; this is in accordance with the weaker diffraction peak (002) compared to the B-CN. Moreover, there were numerous nanopores in the produced  $g\text{-C}_3\text{N}_4$  once the melamine was protonated by  $\text{H}_2\text{SO}_4$  for two hours before it was used as the reactant of the thermal polymerization

reaction. When the melamine is both protonated by  $\text{H}_2\text{SO}_4$  and annealed under the  $\text{N}_2/\text{H}_2$  atmosphere, the prepared sample shows the most porous structure compared to all other samples. The porous structure of P-CN and PH-CN is consistent with their weaker (100) diffraction peak, which indicates the destruction of the in-plane structural packing motif. Commonly, for a nanoparticle sample, the smaller the average particle is, the higher the surface area is. Notably, the quantity and size of the nanopores are crucial for practical applications such as the  $\text{H}_2$  production application.

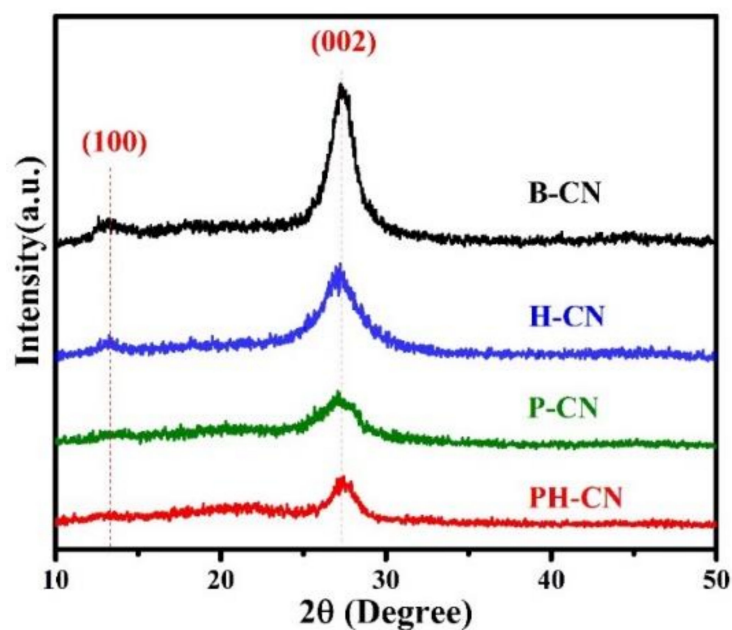


Figure 1. X-ray diffraction patterns of B-CN, H-CN, P-CN, PH-CN.

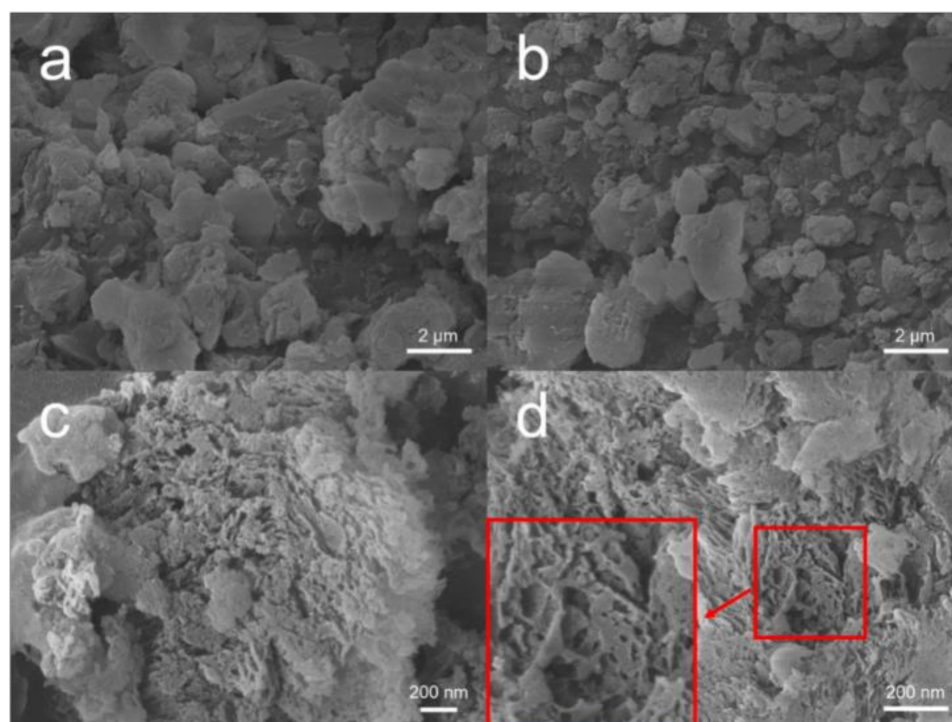
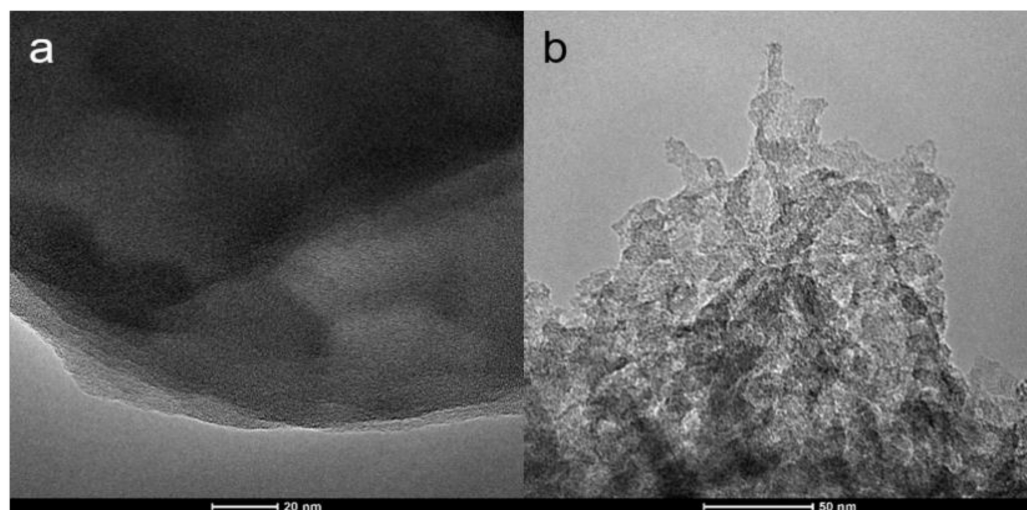


Figure 2. SEM images of (a) B-CN, (b) H-CN, (c) P-CN, (d) PH-CN.

### 2.3. TEM Pattern of the Prepared Samples

From transmission electron microscopy (TEM) images, further insight about the morphology of the samples was obtained. As shown in Figure 3, multi-layered  $g\text{-C}_3\text{N}_4$  was observed in B-CN, and a sponge-like structure, which showed the framework to be fabricated by many small pieces of  $g\text{-C}_3\text{N}_4$ , was found in PH-CN. It could clearly be observed that the PH-CN was exfoliated into thinner nanosheets compared to B-CN and its partial flat sheet-like structure, which could provide plenty of pores and thus enlarge the surface area of the sample.



**Figure 3.** TEM images of (a) B-CN, (b) PH-CN.

### 2.4. BET Images of the Obtained Products/Nitrogen Adsorption

Commonly, a photocatalyst with a larger surface area can provide more active sites for absorption and photoreaction, resulting in an enhanced water splitting reaction. To measure the detailed information of the nanoporous structure, surface area, average pore volume, and pore size distribution was analyzed. Figure 4a shows the  $\text{N}_2$  adsorption–desorption isotherms of the obtained samples. It could be observed that the hysteresis loop of all samples was type H3, suggesting the presence of slit-like pores which had formed between the nanosheets of  $g\text{-C}_3\text{N}_4$ . By contrast, the nitrogen adsorption–desorption amounts of the H-CN, P-CN, and PH-CN increased compared to those of the B-CN (PH-CN > P-CN > H-CN). The Brunauer–Emmett–Teller (BET) measurement of the PH-CN sample shows the largest specific surface area of  $150.1 \text{ m}^2 \text{ g}^{-1}$  and a pore volume of  $0.65 \text{ cm}^3 \text{ g}^{-1}$  (Table 1), suggesting that the effectively enhanced porous structure remarkably improved the surface area of the sample. In addition, it can be observed that the surface area of the sample shows a regular enhancement between each product. By contrast, the surface area of H-CN is about twice of that of B-CN, while the surface area of PH-CN is about twice of that of P-CN. This could be attributed to fewer stacked layers due to the annealing of melamine under  $\text{N}_2/\text{H}_2$  atmosphere. Moreover, this regular enhancement also took place between P-CN and B-CN ( $70.9 \text{ m}^2/\text{g}$  and  $10.9 \text{ m}^2/\text{g}$ ), PH-CN and H-CN ( $150.1 \text{ m}^2/\text{g}$  and  $25.1 \text{ m}^2/\text{g}$ ), which is about seven times larger. This could be attributed to the porous structure which lead to the stable improvement of the surface area derived from protonating the melamine. From Figure 4b, the pore size distribution of the P-CN and PH-CN, which was calculated using the BJH method, indicates the presence of mesopores. To be specific, a sharp peak at 3.4 nm and a broad peak range from 12 nm to 54 nm were found. The numerous mesopores lead to plenty of active sites, allowing for increased absorption of water molecules and being of benefit for mass transfer and charge carrier migration during the hydrogen generation process.



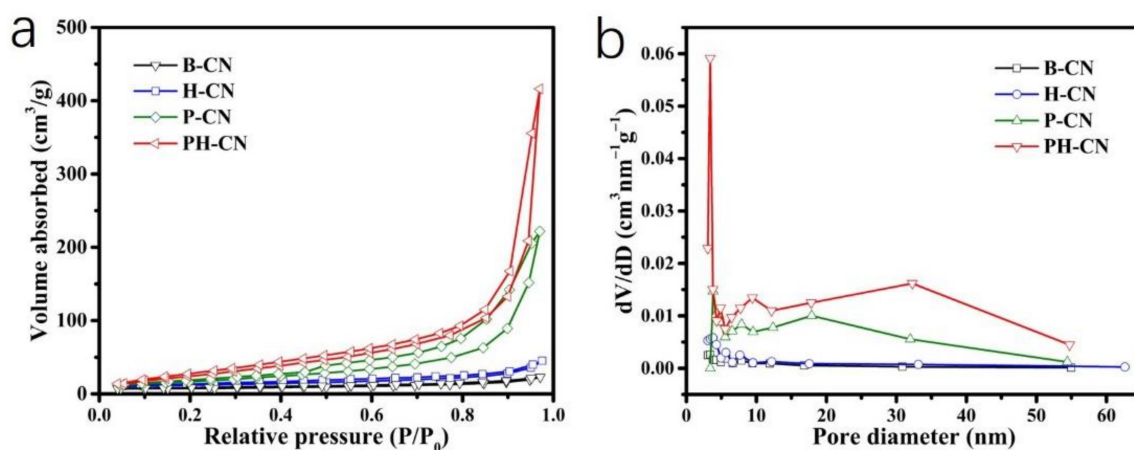


**Figure 4.** (a) Nitrogen adsorption–desorption isotherms, and (b) Pore size distributions using the BJH method for B-CN, H-CN, P-CN, PH-CN.

**Table 1.** Textural properties for B-CN, H-CN, P-CN, PH-CN.

Sample	Specific Surface Area (m <sup>2</sup> /g)	Pore Volume (cm <sup>3</sup> /g)
B-CN	10.9	0.026
H-CN	25.1	0.055
P-CN	70.9	0.359
PH-CN	150.1	0.651

### 2.5. FT-IR Pattern of the Prepared Samples

FT-IR measurement was introduced to further investigate the structure of the synthesized samples. The results are shown in Figure 5. The FT-IR spectrum of B-CN contains some major peaks ranging from 600 cm<sup>-1</sup> to 1800 cm<sup>-1</sup>. This result is consistent with the g-C<sub>3</sub>N<sub>4</sub> features in the previous report [26]. The peak located at 806 cm<sup>-1</sup> is the characteristic breathing mode of tri-s-triazine rings units, and the peaks between 1000 cm<sup>-1</sup> and 1700 cm<sup>-1</sup> are assigned to the typical stretching modes of C-N heterocycles [27]. In addition, the broad peak at around 2900–3600 cm<sup>-1</sup> is assigned to the typical stretching mode of N-H. Besides, there are two small peaks around 2800–3000 cm<sup>-1</sup> for B-CN, P-CN, and PH-CN except H-CN, which may be ascribed to the stretching mode of C-H. Hence, it can be inferred that directly annealing the melamine under N<sub>2</sub>/H<sub>2</sub> atmosphere could restrain the formation of the stretching mode of C-H. Compared to the PH-CN, the protonated process for melamine could promote the formation of the stretching mode of C-H. It can be seen that all four samples possess almost the same peaks, indicating that the chemical structures are similar.

### 2.6. UV-Vis Spectra of the Prepared Samples

To study the optical properties of the prepared products, the UV-vis diffuse reflectance spectra (DRS) was introduced. It is noted that all the four samples show good light harvesting ability. Furthermore, the corresponding band gaps of the samples were estimated. As presented in Figure 6a, the four samples exhibit the intrinsic semiconductor-like absorption spectra. The UV-vis spectra of H-CN, P-CN, and PH-CN display a gradual blue shift compared to the spectrum of B-CN. This phenomenon is derived from the quantum size effect since the layers of obtained product become thinner and they are able to reach the nanoscale. It is clear from Table 2 that the band gaps calculated from the (F(R)\*E)<sup>2</sup> vs. photo energy (E) plots are ca. 2.66 eV (B-CN), 2.75 eV (H-CN), 2.78 eV (P-CN), and 2.89 eV (PH-CN). The conduction band and valence band potentials, denoted as E<sub>CB</sub> and E<sub>VB</sub>, can be calculated by the following empirical equations:

$$E_{CB} = E_{VB} - E_g \quad (1)$$

$$E_{VB} = X - E_e + 0.5E_g \quad (2)$$

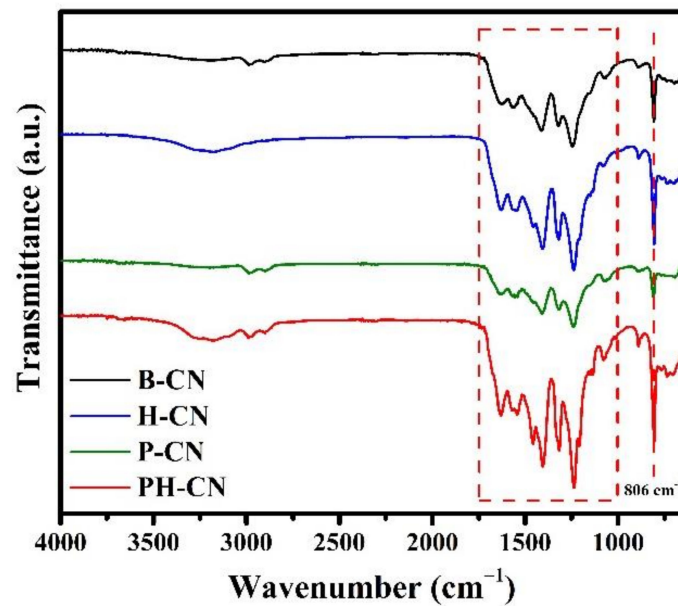


Figure 5. FT-IR spectra of B-CN, H-CN, P-CN, and PH-CN.

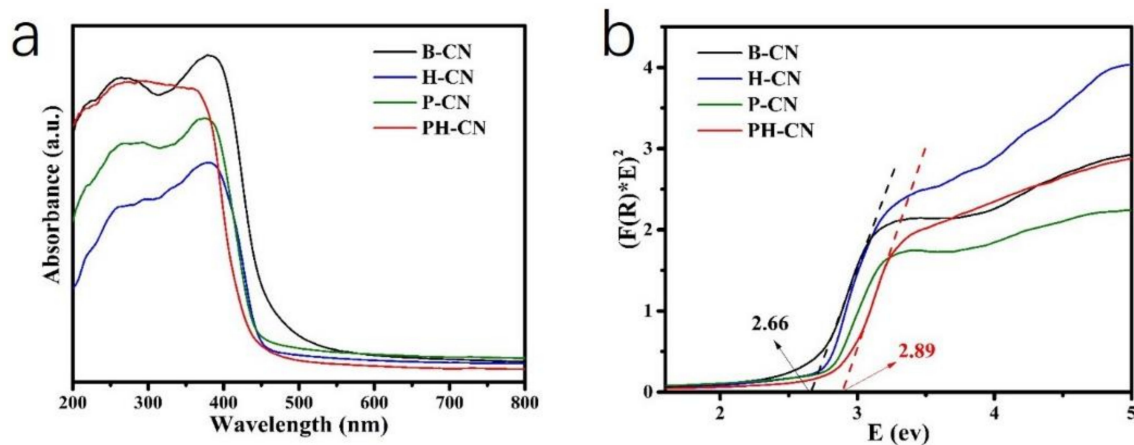


Figure 6. (a) UV-vis diffuse reflectance spectra, and (b) plots of  $(F(R)^3E)^2$  vs. energy (E) for B-CN, H-CN, P-CN, PH-CN.

**Table 2.** The estimated values of band gap energy, valence band potential (vs. NHE), and conduction band potential (vs. NHE) for B-CN, H-CN, P-CN, PH-CN.

Samples	Band Gap Energy (eV)	Valence Band Potential (eV)	Conduction Band Potential (eV)
B-CN	2.66	1.50	−1.16
H-CN	2.75	1.55	−1.20
P-CN	2.78	1.56	−1.22
PH-CN	2.89	1.62	−1.27

In the above equations, X is the absolute electronegativity of the semiconductor and X for the g-C<sub>3</sub>N<sub>4</sub> is 4.67 eV. E<sub>e</sub> is the energy of free electrons on the hydrogen scale (about 4.5 eV). The estimated VB and CB potentials are presented in Table 2. From Table 2, it can be found that the CB potential of PH-CN is higher than that of B-CN, while the VB potential

is lower. This finding illustrates that the redox ability of the charge carriers generated in PH-CN are improved, which favors the enhancement of the photocatalytic ability.

### 2.7. XPS Spectra of the Prepared Samples

The chemical valence states and chemical composition of the samples were further analyzed by X-ray photoelectron spectroscopy (XPS). The positions of all measured peaks were calibrated by the binding energy of C 1s (284.8 eV). The XPS spectra (Figure 7a) show that C 1s, N 1s, and O 1s peaks are present in the sample. Additional peak O 1s may be attributed to the surface-absorbed water molecules. The XPS valence band spectra are mainly used to characterize the distance between the Fermi energy level and the valence band of a semiconductor. Figure 7b shows XPS valence band spectra of B-CN and PH-CN, respectively. The valence band spectrum value ( $E_{VB-XPS}$ ) of B-CN and PH-CN are 2.55 and 2.71 eV, respectively. Combined with the band gap energy, valence band potential, and conduction band potential shown in Table 2, the energy level diagram of B-CN and PH-CN can be presented in Figure 8. The increased Fermi level and conduction band potential are a benefit for water reduction, while the decreased valence band potential could promote water oxidation. Figure 7c displays the high-resolution XPS spectra of C 1s for the prepared B-CN and PH-CN, in which both the peaks at 284.8 eV for B-CN and PH-CN should be due to the graphitic C=C or/and the cyano group or/and adventitious carbon in the sample [30–32], and the 288.48 eV peak should be ascribed to the CN network [33,34]. The peak intensity ratio between 284.8 eV and 288.48 eV of C 1s of B-CN and PH-CN decreased sharply from more than one to less than one, which indicates that the melamine protonated and subsequently annealed under  $N_2/H_2$  atmosphere could promote the CN network constructed and reduce the graphitic C=C or/and adventitious carbon in the sample. This moderate removal of carbon impurities is helpful for the optimization of the aromatic p-conjugated system for charge separation, since too many graphitic carbon centers doped in the CN conjugated system will act as defect centers for charge recombination [35]. The high-resolution XPS spectra of N 1s for the prepared B-CN and PH-CN is displayed in Figure 7d. Both deconvolution peaks at 398.99 and 400.59 eV for B-CN and 398.94 and 400.59 eV for PH-CN should be ascribed to the  $sp^2$  N atoms in the triazine units, bridging N in N-(C)3 or N-H [30,34]. Moreover, the additional peak for PH-CN, located at 404.48 eV, is attributed to N in the heterocycles and cyano groups [34]. Conversely, the peak intensity ratio between 398.99 eV and 400.59 eV for B-CN, and 398.94 eV and 400.59 eV for PH-CN of N 1s, increased greatly, which could be attributed to the promoted CN network construction, as discussed above.

### 2.8. Photocatalytic Hydrogen Production Performance

The photocatalytic hydrogen production performance was explored in aqueous solution containing triethanolamine as a hole sacrificial reagent which could lower the recombination rate of photogenerated electron pairs by consuming the photoinduced holes under solar light irradiation. Moreover, 3 wt% of Pt was employed in the aqueous solution as a co-catalyst after having been in situ and photodeposited onto the surface of the sample. As demonstrated in Figure 9a,b, H-CN exhibits a superior hydrogen evolution rate (HER) of  $720.3 \mu\text{mol h}^{-1} \text{g}^{-1}$  compared to poor HER ( $414.8 \mu\text{mol h}^{-1} \text{g}^{-1}$ ) of B-CN, which could be attributed to its smaller nanosheets, as can be clearly observed in the SEM images. Smaller nanosheets can provide more active sites due to their larger surface area. Additionally, it is noted that the P-CN exhibits remarkably superior HER of  $2179.1 \mu\text{mol h}^{-1} \text{g}^{-1}$  in comparison with B-CN, since the melamine is protonated by  $H_2SO_4$  for 2 h before calcination for P-CN, which performed loose structure. Remarkably, PH-CN showed optimal photocatalytic activity with the HER of  $4104.2 \mu\text{mol h}^{-1} \text{g}^{-1}$ , which was about 10 times higher than that of B-CN. This phenomenon further suggests the smaller and thinner nanosheets of the  $g\text{-C}_3\text{N}_4$  with a sponge-like structure favor the significant enhancement of photocatalytic hydrogen production performance. The cyclic stability performance for the photocatalytic  $H_2$  evolution over 3 wt% of Pt-deposited PH-CN is shown in Figure 10.

The PH-CN maintains a high H<sub>2</sub> production rate (which is about 87% of initial HER) after five photocatalytic reactions.

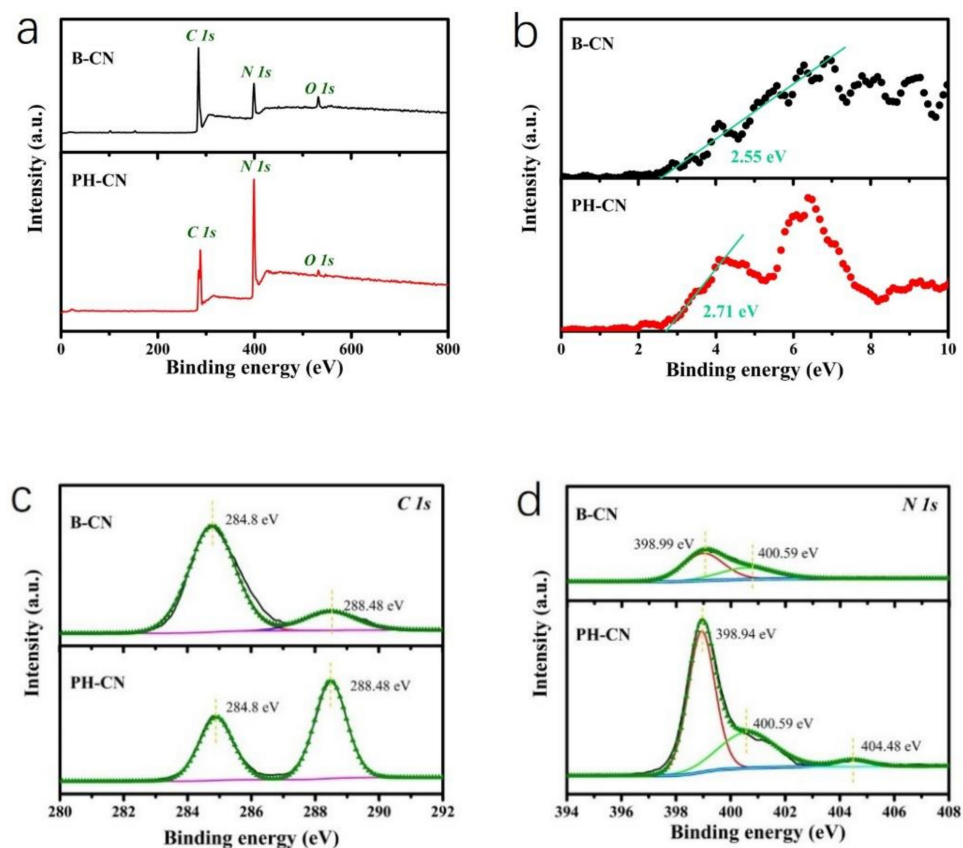


**Figure 7.** (a) XPS survey spectra of B-CN and PH-CN, (b) valence band spectrum of B-CN and PH-CN, and (c,d) high-resolution XPS spectra of C 1s and N 1s for B-CN and PH-CN.

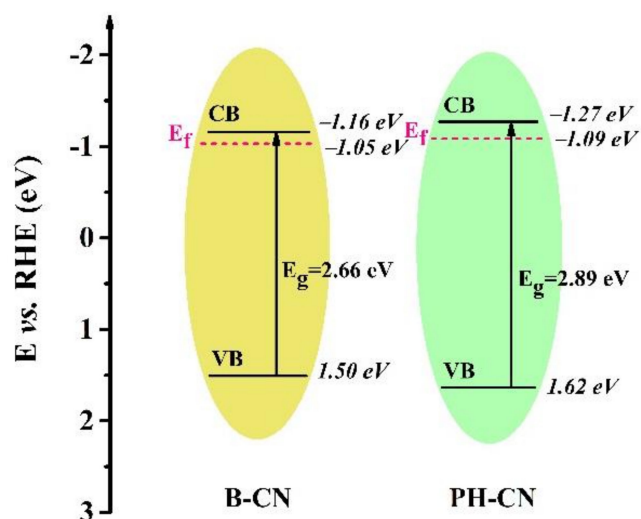


**Figure 8.** The energy level diagram of B-CN and PH-CN.



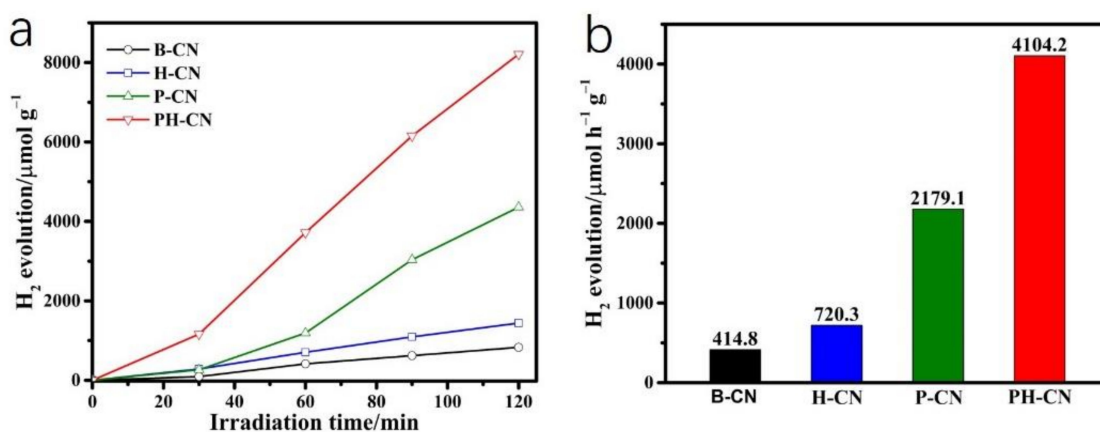


**Figure 9.** (a) Time-dependent photocatalytic generation of hydrogen, and (b) hydrogen evolution rate over different samples under solar light irradiation (AM 1.5G).

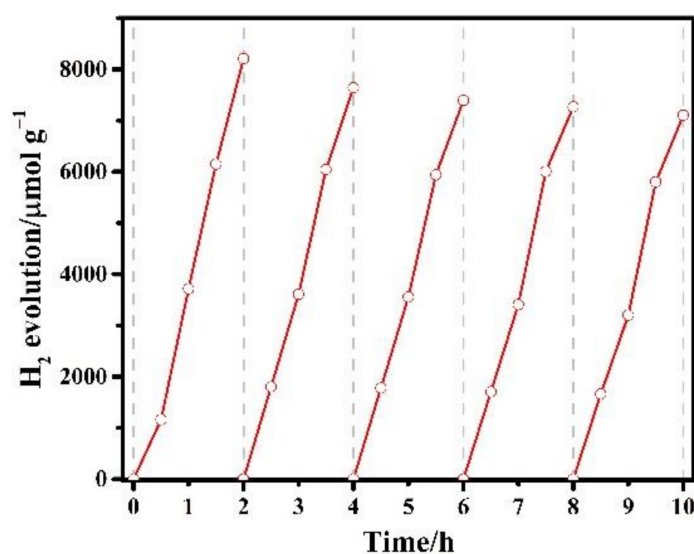


**Figure 10.** Cyclic stability tests for the photocatalytic H<sub>2</sub> production over PH-CN under solar light irradiation (AM 1.5G).

### 2.9. PL Spectra and Photoelectrochemical Properties

The photoluminescence (PL) spectra of the obtained products were tested at an excitation wavelength of 270 nm to investigate the photogenerated charge carrier performance of trapping, migration, and recombination. As can be seen in Figure 11, the B-CN presents a broad emission peak at ca. 466 nm, which is consistent with the band gap of 2.66 eV, as shown by UV-vis diffraction spectra in Figure 6a,b. It can be observed that the peak of PH-CN shows a significant blue shift compared to that of B-CN, which matches well with the UV-vis result above. Additionally, it is noted that annealing the precursor under N<sub>2</sub>/H<sub>2</sub> atmosphere contributes to the blue shift of the photoluminescence emission peaks and increases the peak intensity. It is believed that the higher peak intensity of H-CN compared with B-CN and PH-CN compared with P-CN is derived from a larger number of emission centers, which is due to the lower degree of polycondensation [36]. The emission center may be attributed to some defect state, which could promote photocatalytic activity. The tendency for varying intensity of PL in the obtained samples is inconsistent with their photocatalytic hydrogen production activity. Thus, the photogenerated electron-hole pairs' separation efficiency should not be estimated only by PL intensity for the prepared samples in this work.

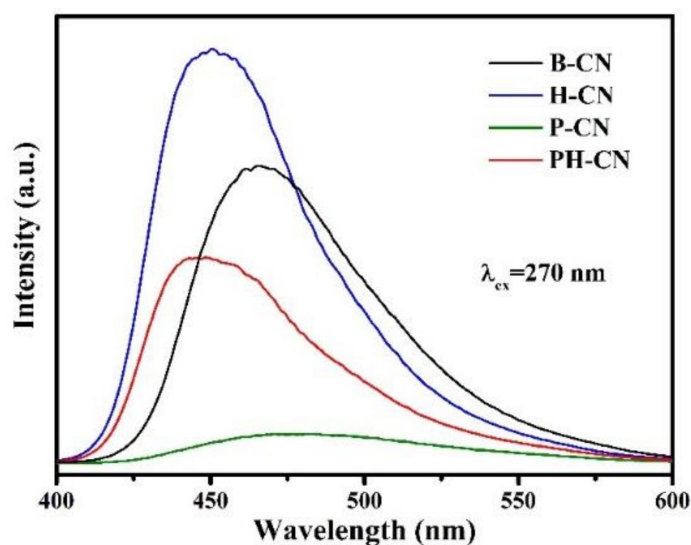


Figure 11. Photoluminescence (PL) spectra for B-CN, H-CN, P-CN, and PH-CN.

Electrochemical performance is also an important factor for enhanced photocatalytic activity. As shown in Figure 12a, the photocurrent density of PH-CN, P-CN, H-CN, and B-CN is 1.72, 1.18, 1.05, and 0.71  $\mu\text{A}/\text{cm}^2$ . The photocurrent density of PH-CN is approximately 1.46, 1.63, and 2.42 times higher than that of P-CN, H-CN, and B-CN, implying a better separation and effective migration of charge carriers. Owing to the increased transfer rate of photogenerated carriers, the PH-CN performs a minor radius within EIS results compared to P-CN, H-CN, and B-CN (Figure 12b). On the one hand, the photogenerated carriers could effectively separate on the surface and easily migrate to the surface as a result of the thin  $\text{g-C}_3\text{N}_4$  nanosheets. On the other hand, the  $\text{g-C}_3\text{N}_4$  nanosheets edge is more active compared to other areas, and the high surface area and porous structure of PH-CN could provide more active sites for water reduction.

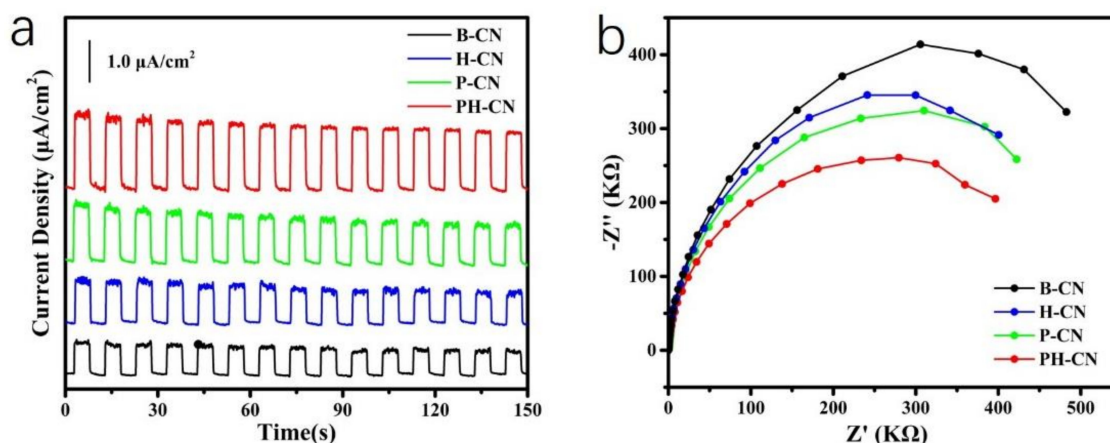


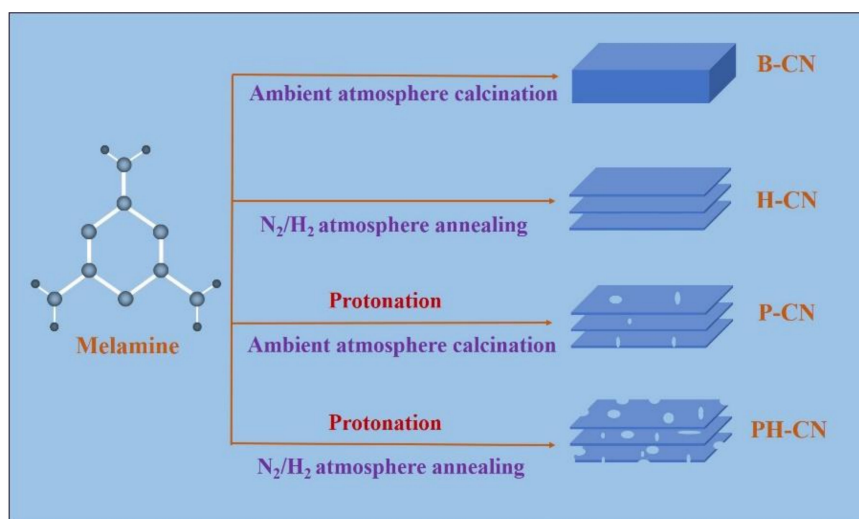
Figure 12. (a) Transient photocurrent density J-t curves at 0.5 V vs. Ag/AgCl, and (b) EIS curves for the prepared B-CN, H-CN, P-CN, and PH-CN.

### 3. Materials and Methods

#### 3.1. Materials

All chemicals and reagents for synthesis and analysis were analytically graded without further purification for use. Melamine ( $\text{C}_3\text{H}_6\text{N}_6$ ) was purchased from Tianjin Damao Chemical Reagent Factory (Tianjin, China). Sulfuric acid ( $\text{H}_2\text{SO}_4$ ) was purchased from Chengdu Chron Chemicals Co., Ltd (Chengdu, China). Triethanolamine ( $\text{C}_6\text{H}_{15}\text{NO}_3$ ) was purchased from Tianjin Hongyan Chemical Reagent Factory (Tianjin, China). Hexachloroplatinic

acid hexahydrate ( $\text{H}_2\text{PtCl}_6 \cdot 6\text{H}_2\text{O}$ ) was purchased from Sinopharm Chemical Reagent Co., Ltd (Shanghai, China). Anhydrous sodium sulfate ( $\text{Na}_2\text{SO}_4$ ) was purchased from Tianjin GuangFu Technology Development Co., Ltd (Tianjin, China). Ethanol ( $\text{C}_2\text{H}_6\text{O}$ ) was purchased from Tianjin Fuyu Fine Chemical Co., Ltd. The distilled water was prepared by ULUPURE UPR-II-20L water purification system. In this work, pristine melamine and protonated melamine were calcined under ambient atmosphere or annealed under  $\text{N}_2/\text{H}_2$  (95%  $\text{N}_2$ , 5%  $\text{H}_2$ ) atmosphere, respectively, as shown in Scheme 1. Detailed information is as follows.



**Scheme 1.** Schematic illustration of preparing B-CN, H-CN, P-CN, PH-CN under different conditions.

### 3.2. Preparation of Bulk $g\text{-C}_3\text{N}_4$

The bulk  $g\text{-C}_3\text{N}_4$  was prepared via calcination of the melamine in the tube furnace under ambient atmosphere (B-CN). Specifically, 5 g of melamine in a ceramic crucible was heated at  $550\text{ }^\circ\text{C}$  for 3 h under ambient atmosphere and the heating rate of this thermal polymerization reaction was  $10\text{ }^\circ\text{C}/\text{min}$ . After naturally cooling down to room temperature, the yellow product was collected and ground into powder.

### 3.3. Preparation of $g\text{-C}_3\text{N}_4$ Nanosheets

The  $g\text{-C}_3\text{N}_4$  nanosheets were prepared via annealing of the melamine in the tube furnace under  $\text{N}_2/\text{H}_2$  (95%  $\text{N}_2$ , 5%  $\text{H}_2$ ) atmosphere (H-CN). In detail, 5 g of melamine in a ceramic crucible was heated at  $550\text{ }^\circ\text{C}$  for 3 h under  $\text{N}_2/\text{H}_2$  atmosphere and the heating rate of this thermal polymerization reaction was  $10\text{ }^\circ\text{C}/\text{min}$ . After naturally cooling down to room temperature, the sample was collected and ground into powder.

### 3.4. Preparation of Porous Structure $g\text{-C}_3\text{N}_4$ Nanosheets

The porous structure  $g\text{-C}_3\text{N}_4$  nanosheets were synthesized via calcination of the protonated melamine under ambient atmosphere (P-CN). To be specific, 5 g of melamine was slowly put in the sulfuric acid aqueous solution (the volume ratio of  $\text{H}_2\text{SO}_4$  and  $\text{H}_2\text{O}$  is 1:9), followed by vigorously stirring for two hours, centrifuging the mixture at 3000 r/min for 5 min, washing the product with ethanol and distilled water several times, and drying the product at  $60\text{ }^\circ\text{C}$  overnight. Finally, 5 g of the product was heated at  $550\text{ }^\circ\text{C}$  for 3 h under ambient atmosphere and the heating rate of this thermal polymerization reaction was  $10\text{ }^\circ\text{C}/\text{min}$ . After naturally cooling down to room temperature, the sample was collected and ground into powder.

### 3.5. Preparation of Sponge-Like $g\text{-C}_3\text{N}_4$ Nanosheets

The sponge-like  $g\text{-C}_3\text{N}_4$  nanosheets were synthesized via annealing of the protonated melamine under  $\text{N}_2/\text{H}_2$  (95%  $\text{N}_2$ , 5%  $\text{H}_2$ ) atmosphere (PH-CN). In detail, 5 g of the

protonated melamine was heated at 550 °C for 3 h under N<sub>2</sub>/H<sub>2</sub> atmosphere and the heating rate of this thermal polymerization reaction was 10 °C/min. After naturally cooling down to room temperature, the sample was collected and ground into powder.

### 3.6. Characterization

The crystal structure of the samples was identified by X-ray diffraction (XRD) on a Shimadzu XRD-6000 powder diffractometer (Shimadzu, Tokyo, Japan) with Cu K $\alpha$  radiation ( $\lambda = 0.15406$  nm), operating at 40 kV (0.02°/s) in the 2 $\theta$  range of 10–50°. Fourier transform infrared (FT-IR) spectroscopy was recorded on a PerkinElmer FT-IR spectrophotometer (PerkinElmer Frontier, PerkinElmer, Waltham, MA, USA) to infer the molecular structural information of the samples. A transmission electron microscope (TEM, Tecnai G2 F20 S-twin field emission transmission, FEI, Hillsboro, OR, USA) and a JSM-6390A scanning electron microscope (SEM, JEOL, Tokyo, Japan) were used to investigate the microstructure and micromorphology of the samples. The diffuse reflectance UV-vis absorption spectra of the photoelectrodes were characterized using a PerkinElmer Lambda 950 UV-vis-NIR spectrophotometer (PerkinElmer, Waltham, MA, USA). The chemical composition and chemical valence state of products were analyzed using X-ray photoelectron spectroscopy (XPS, ULVAC-PHI, PHI5000 VersaProbeIII spectrometer, ULVAC-PHI, Chigasaki, Japan). The BET surface areas were collected using a Quantachrome NOVA 2000e sorption analyzer (Quantachrome, Boynton Beach, FL, USA) based on N<sub>2</sub> adsorption–desorption isotherm at 77 K after the samples were degassed at 300 °C for 5 h. The photoluminescence (PL) emission spectra were tested by using a Hitachi-F7000 fluorescence spectrophotometer (Hitachi, Tokyo, Japan).

### 3.7. Photocatalytic Measurement

The photocatalytic hydrogen evaluation was carried out under a new on-line analysis system (Beijing Perfect Light Technology Co. Ltd., Beijing, China, LabSolar-IIIAG) and irradiated under solar light AM 1.5G illumination. For each reaction, a total of 0.1 g of photocatalyst powder was added into 50 mL of aqueous solution containing 10 vol% triethanolamine sacrificial agent and 3 wt% Pt (H<sub>2</sub>PtCl<sub>6</sub>·6H<sub>2</sub>O at the precursor of the cocatalyst). Additionally, the hydrogen evaluation system was evacuated for 30 min prior to the irradiation using the 300 W Xe lamp, followed by periodically recording the amount of produced H<sub>2</sub> by gas chromatography (GC-7900, Techcomp, Shanghai, China).

### 3.8. Photoelectrochemical Measurement

The photoelectrochemical (PEC) performance of the samples was measured in a three-electrode cell using an electrochemical working station (Princeton Versa STAT 4, AMETEK, Berwyn, PA, USA) under AM 1.5G illumination. All measurements were performed in a neutral electrolyte solution (0.5 M Na<sub>2</sub>SO<sub>4</sub>, PH = 7.0). A Pt mesh, Ag/AgCl electrode and samples were as the counter electrode (CE), reference electrode (RE) and working electrode (WE) in the three-electrode cell. The electrochemical impedance spectra (EIS) were measured at open circuit condition with the frequency range of 0.01 Hz to 100 kHz under AM 1.5G light illumination. The photoelectrode was synthesized through dropping the dispersion containing 5 mg of sample, ethanol, and water onto the fluorine-tin-oxide (FTO) conductive glass.

## 4. Conclusions

In summary, we have succeeded in synthesizing sponge-like g-C<sub>3</sub>N<sub>4</sub> nanosheets (PH-CN) with a porous structure by annealing the protonated melamine under N<sub>2</sub>/H<sub>2</sub> atmosphere. The architecture endows g-C<sub>3</sub>N<sub>4</sub> nanosheets with a larger surface area (150.1 m<sup>2</sup>/g) and fewer stacked layers, which not only means will there be more active sites but also demonstrates that the ability to harvest light will be improved; this will, in turn, benefit photocatalytic hydrogen evolution performance. The obtained PH-CN sample exhibits remark-

ably enhanced photocatalytic hydrogen evolution activity (a HER of  $4104 \mu\text{mol h}^{-1} \text{g}^{-1}$ ), which is nearly 10 times higher than B-CN.

**Author Contributions:** C.W.: Conceptualization, Investigation, Methodology, Writing—Original Draft. T.H.: Investigation, Methodology, Formal analysis. C.X.: Investigation, Validation. H.M.: Conceptualization, Resources, Writing—Review and editing, Supervision, Funding acquisition. All authors have read and agreed to the published version of the manuscript.

**Funding:** This research was funded by the National Natural Science Foundation of China, grant number 11804274.

**Data Availability Statement:** Data are contained within the article.

**Conflicts of Interest:** The authors declare no conflict of interest.

## References

1. Dawood, F.; Anda, M.; Shafiullah, G.M. Hydrogen production for energy: An overview. *Int. J. Hydrog. Energy* **2020**, *45*, 3847–3869. [[CrossRef](#)]
2. Nikolaidis, P.; Poullikkas, A. A comparative overview of hydrogen production processes. *Renew. Sustain. Energy Rev.* **2017**, *67*, 597–611. [[CrossRef](#)]
3. Zhang, L.; Li, Y.; Li, C.; Chen, Q.; Zhen, Z.; Jiang, X.; Zhong, M.; Zhang, F.; Zhu, H. Scalable low-band-gap  $\text{Sb}_2\text{Se}_3$  thin-film photocathodes for efficient visible-near-infrared solar hydrogen evolution. *ACS Nano* **2017**, *11*, 12753–12763. [[CrossRef](#)]
4. Fujishima, A.; Honda, K. Electrochemical photolysis of water at a semiconductor electrode. *Nature* **1972**, *238*, 37–38. [[CrossRef](#)] [[PubMed](#)]
5. Rahman, M.Z.; Kibria, M.G.; Mullins, C.B. Metal-free photocatalysts for hydrogen evolution. *Chem. Soc. Rev.* **2020**, *49*, 1887–1931. [[CrossRef](#)] [[PubMed](#)]
6. Yao, Y.; Gao, X.Y.; Li, Z.Z.; Meng, X.C. Photocatalytic reforming for hydrogen evolution: A review. *Catalysts* **2020**, *10*, 335. [[CrossRef](#)]
7. Patnaik, S.; Sahoo, D.P.; Parida, K. Recent advances in anion doped  $\text{g-C}_3\text{N}_4$  photocatalysts: A review. *Carbon* **2021**, *172*, 682–711. [[CrossRef](#)]
8. Wu, C.; Xue, S.; Qin, Z.; Nazari, M.; Yang, G.; Yue, S.; Tong, T.; Ghasemi, H.; Hernandez, F.R.; Xue, S.; et al. Making  $\text{g-C}_3\text{N}_4$  ultra-thin nanosheets active for photocatalytic overall water splitting. *Appl. Catal. B Environ.* **2021**, *282*, 119557. [[CrossRef](#)]
9. Cui, J.; Luo, Y.; Dong, B.; Qi, Y.; Jia, M.; Zhang, F.; Li, C. Investigation on the influence of Sc ions doping on the structure and performance of  $\text{Ta}_3\text{N}_5$  photocatalyst for water oxidation under visible light irradiation. *Solar RRL* **2020**, *4*, 1900445. [[CrossRef](#)]
10. Doustkhah, E.; Assadi, M.N.; Komaguchi, K.; Tsumoji, N.; Esmat, M.; Fukata, N.; Tomita, O.; Abe, R.; Ohtani, B.; Ide, Y. In situ blue titania via band shape engineering for exceptional solar  $\text{H}_2$  production in rutile  $\text{TiO}_2$ . *Appl. Catal. B Environ.* **2021**, *297*, 120380. [[CrossRef](#)]
11. Cai, X.; Huang, Y.; Hu, J.; Zhu, S.; Tian, X.; Zhang, K.; Ji, G.; Zhang, Y.; Fu, Z.; Tan, C. Tuning photocatalytic performance of multilayer ZnO for water splitting by biaxial strain composites. *Catalysts* **2020**, *10*, 1208. [[CrossRef](#)]
12. Wang, Y.; Huang, H.; Zhang, Z.; Wang, C.; Yang, Y.; Li, Q.; Xu, D. Lead-free perovskite  $\text{Cs}_2\text{AgBiBr}_6/\text{g-C}_3\text{N}_4$  Z-scheme system for improving  $\text{CH}_4$  production in photocatalytic  $\text{CO}_2$  reduction. *Appl. Catal. B Environ.* **2021**, *282*, 119570. [[CrossRef](#)]
13. Cheng, L.; Yin, H.; Cai, C.; Fan, J.; Xiang, Q. Single Ni atoms anchored on porous few-layer  $\text{g-C}_3\text{N}_4$  for photocatalytic  $\text{CO}_2$  reduction: The role of edge confinement. *Small* **2020**, *16*, 2002411. [[CrossRef](#)]
14. Zhang, X.; Kim, D.; Yan, J.; Lee, L.Y.S. Photocatalytic  $\text{CO}_2$  reduction enabled by interfacial S-Scheme heterojunction between ultrasmall copper phosphosulfide and  $\text{g-C}_3\text{N}_4$ . *ACS Appl. Mater. Interfaces* **2021**, *13*, 9762–9770. [[CrossRef](#)]
15. Yang, C.; Tan, Q.; Li, Q.; Zhou, J.; Fan, J.; Li, B.; Sun, J.; Lv, K. 2D/2D  $\text{Ti}_3\text{C}_2$  MXene/ $\text{g-C}_3\text{N}_4$  nanosheets heterojunction for high efficient  $\text{CO}_2$  reduction photocatalyst: Dual effects of urea. *Appl. Catal. B Environ.* **2020**, *268*, 118738. [[CrossRef](#)]
16. Zhou, X.; Fang, Y.; Cai, X.; Zhang, S.; Yang, S.; Wang, H.; Zhong, X.; Fang, Y. In situ photodeposited construction of Pt-CdS/ $\text{g-C}_3\text{N}_4$ - $\text{MnO}_x$  composite photocatalyst for efficient visible-light-driven overall water splitting. *ACS Appl. Mater. Interfaces* **2020**, *12*, 20579–20588. [[CrossRef](#)]
17. Shi, W.; Li, M.; Huang, X.; Ren, H.; Yan, C.; Guo, F. Facile synthesis of 2D/2D  $\text{Co}_3(\text{PO}_4)_2/\text{g-C}_3\text{N}_4$  heterojunction for highly photocatalytic overall water splitting under visible light. *Chem. Eng. J.* **2020**, *382*, 122960. [[CrossRef](#)]
18. Miao, H.; Zhang, G.; Hu, X.; Mu, J.; Han, T.; Fan, J.; Zhu, C.; Song, L.; Bai, J.; Hou, X. A novel strategy to prepare 2D  $\text{g-C}_3\text{N}_4$  nanosheets and their photoelectrochemical properties. *J. Alloys Compd.* **2017**, *690*, 669–676. [[CrossRef](#)]
19. Lin, T.H.; Chang, Y.H.; Chiang, K.P.; Wang, J.C.; Wu, M.C. Nanoscale multidimensional Pd/ $\text{TiO}_2/\text{g-C}_3\text{N}_4$  catalyst for efficient solar-driven photocatalytic hydrogen production. *Catalysts* **2021**, *11*, 59. [[CrossRef](#)]
20. Guo, F.; Huang, X.; Chen, Z.; Sun, H.; Chen, L. Prominent co-catalytic effect of CoP nanoparticles anchored on high-crystalline  $\text{g-C}_3\text{N}_4$  nanosheets for enhanced visible-light photocatalytic degradation of tetracycline in wastewater. *Chem. Eng. J.* **2020**, *395*, 125118. [[CrossRef](#)]



21. Chen, C.; Xie, M.; Kong, L.; Lu, W.; Feng, Z.; Zhan, J. Mn<sub>3</sub>O<sub>4</sub> nanodots loaded g-C<sub>3</sub>N<sub>4</sub> nanosheets for catalytic membrane degradation of organic contaminants. *J. Hazard. Mater.* **2020**, *390*, 122146. [[CrossRef](#)]
22. Sun, P.; Liu, H.; Feng, M.; Zhai, Z.; Fang, Y.; Zhang, X.; Sharma, V.K. Strategic combination of N-doped graphene and g-C<sub>3</sub>N<sub>4</sub>: Efficient catalytic peroxydisulfate-based oxidation of organic pollutants by non-radical-dominated processes. *Appl. Catal. B Environ.* **2020**, *272*, 119005. [[CrossRef](#)]
23. Yan, S.C.; Li, Z.S.; Zou, Z.G. Photodegradation performance of g-C<sub>3</sub>N<sub>4</sub> fabricated by directly heating melamine. *Langmuir* **2009**, *25*, 10397–10401. [[CrossRef](#)]
24. Zheng, Y.; Liu, J.; Liang, J.; Jaroniec, M.; Qiao, S.Z. Graphitic carbon nitride materials: Controllable synthesis and applications in fuel cells and photocatalysis. *Energy Environ. Sci.* **2012**, *5*, 6717–6731. [[CrossRef](#)]
25. Hong, J.; Xia, X.; Wang, Y.; Xu, R. Mesoporous carbon nitride with in situ sulfur doping for enhanced photocatalytic hydrogen evolution from water under visible light. *J. Mater. Chem.* **2012**, *22*, 15006–15012. [[CrossRef](#)]
26. Fan, X.; Zhang, L.; Cheng, R.; Wang, M.; Li, M.; Zhou, Y.; Shi, J. Construction of graphitic C<sub>3</sub>N<sub>4</sub>-based intramolecular donor–acceptor conjugated copolymers for photocatalytic hydrogen evolution. *ACS Catal.* **2015**, *5*, 5008–5015. [[CrossRef](#)]
27. Martin, D.J.; Qiu, K.; Shevlin, S.A.; Handoko, A.D.; Chen, X.; Guo, Z.; Tang, J. Highly efficient photocatalytic H<sub>2</sub> evolution from water using visible light and structure-controlled graphitic carbon nitride. *Angew. Chem. Int. Ed.* **2014**, *53*, 9240–9245. [[CrossRef](#)]
28. Wu, M.; Gong, Y.; Nie, T.; Zhang, J.; Wang, R.; Wang, H.; He, B. Template-free synthesis of nanocage-like g-C<sub>3</sub>N<sub>4</sub> with high surface area and nitrogen defects for enhanced photocatalytic H<sub>2</sub> evolution activity. *J. Mater. Chem. A* **2019**, *7*, 5324–5332. [[CrossRef](#)]
29. Han, C.; Su, P.; Tan, B.; Ma, X.; Lv, H.; Huang, C.; Wang, P.; Tong, Z.; Li, G.; Huang, Y.; et al. Defective ultra-thin two-dimensional g-C<sub>3</sub>N<sub>4</sub> photocatalyst for enhanced photocatalytic H<sub>2</sub> evolution activity. *J. Colloid Interface Sci.* **2021**, *581*, 159–166. [[CrossRef](#)]
30. Yang, S.; Gong, Y.; Zhang, J.; Zhan, L.; Ma, L.; Fang, Z.; Vajtai, R.; Wang, X.; Ajayan, P.M. Exfoliated graphitic carbon nitride nanosheets as efficient catalysts for hydrogen evolution under visible light. *Adv. Mater.* **2013**, *25*, 2452–2456. [[CrossRef](#)]
31. Li, Y.; Zhang, J.; Wang, Q.; Jin, Y.; Huang, D.; Cui, Q.; Zou, G. Nitrogen-rich carbon nitride hollow vessels: Synthesis, characterization, and their properties. *J. Phys. Chem. B* **2010**, *114*, 9429–9434. [[CrossRef](#)] [[PubMed](#)]
32. Dante, R.C.; Martín, P.; Correa, A.; Martín, J. Synthesis of graphitic carbon nitride by reaction of melamine and uric acid. *Mater. Chem. Phys.* **2011**, *130*, 1094–1102. [[CrossRef](#)]
33. Hou, Y.; Wen, Z.; Cui, S.; Guo, X.; Chen, J. Constructing 2D porous graphitic C<sub>3</sub>N<sub>4</sub> nanosheets/nitrogen-doped graphene/layered MoS<sub>2</sub> ternary nanojunction with enhanced photoelectrochemical activity. *Adv. Mater.* **2013**, *25*, 6291–6297. [[CrossRef](#)] [[PubMed](#)]
34. Li, Y.; Zhang, H.; Liu, P.; Wang, D.; Li, Y.; Zhao, H. Cross-linked g-C<sub>3</sub>N<sub>4</sub>/rGO nanocomposites with tunable band structure and enhanced visible light photocatalytic activity. *Small* **2013**, *9*, 3336–3344. [[CrossRef](#)]
35. Zhang, J.; Zhang, M.; Lin, L.; Wang, X. Sol processing of conjugated carbon nitride powders for thin-film fabrication. *Angew. Chem. Int. Ed.* **2015**, *127*, 6395–6399. [[CrossRef](#)]
36. Tong, Z.; Yang, D.; Shi, J.; Nan, Y.; Sun, Y.; Jiang, Z. Three-dimensional porous aerogel constructed by g-C<sub>3</sub>N<sub>4</sub> and graphene oxide nanosheets with excellent visible-light photocatalytic performance. *ACS Appl. Mater. Interfaces* **2015**, *7*, 25693–25701. [[CrossRef](#)] [[PubMed](#)]